RSC Advances

ROYAL SOCIETY OF CHEMISTRY

PAPER

View Article Online
View Journal | View Issue

Check for updates

Cite this: *RSC Adv.*, 2025, **15**, 41330

High-TMR iron-free double-barrier MTJs with $MoTe_2$ spacing for label-free magnetic biosensors

Tahereh Azargoshasb, Paria Kamkar and Hadi Heidari *

Received 11th July 2025
Accepted 8th September 2025

DOI: 10.1039/d5ra04973c

rsc.li/rsc-advances

Double-barrier magnetic tunnel junctions (DB-MTJs) present a promising platform for biosensing applications due to their improved sensitivity and capability for label-free, non-invasive detection. This work models a high-performance iron-free DB-MTJ configuration: Co_2MnSi–MgO–$MoTe_2$–MgO–Co_2MnSi. By Utilizing density functional theory (DFT) and the nonequilibrium Green's function (NEGF) technique, we computed the tunnelling magnetoresistance (TMR) ratio, transmission spectra, density of states (DOS), and bandgaps for the Co_2MnSi–MgO–$MoTe_2$–MgO–Co_2MnSi system. The DB-MTJ features iron-free Co_2MnSi Heusler alloy electrodes and a $MoTe_2$ transition metal dichalcogenide (TMDC) spacer, achieving a tunneling magnetoresistance (TMR) ratio of 1226%, alongside other configurations with TMR ratios ranging from 22% to 667%. The high TMR, driven by the tunable electronic properties of $MoTe_2$ and the half-metallic nature of Co_2MnSi, enables exceptional sensitivity to interfacial modifications, making it ideal for detecting biomarkers. The application of iron-free materials increases the electrodes' stability and spin polarization and improves the sensitivity of the DB-MTJs upon interface variations. This research points out the high-potential applications of Heusler-based and iron-free DB-MTJ's as sensitive and label-free biosensors.

Introduction

Cancer remains a significant global health challenge, with over a million new cases diagnosed annually. Early detection is critical for improving clinical outcomes, with survival rates increasing by approximately 90% when the disease is identified at an early stage.[1] Conventional diagnostic approaches, such as imaging techniques and tissue biopsy, are limited by several drawbacks, including exposure to ionizing radiation, high procedural costs, and invasiveness. These limitations underscore the urgent need for innovative, non-invasive diagnostic platforms that enable accurate and timely detection. These challenges underscore the crucial requirement for novel, non-invasive diagnostic platforms that can deliver sensitive, specific, and fast cancer biomarker detection.[2,3] New developments in biosensing solutions have been promising in meeting these requirements by making cancer biomarker identification possible through label-free, real-time techniques, presenting a groundbreaking strategy towards cancer diagnostics at the early stage.[4–7] Magnetoresistive (MR) devices, particularly those based on spintronic principles, hold significant promise for early diagnosis and disease monitoring due to their exceptional sensitivity to minute magnetic field variations *via* the tunneling magnetoresistance (TMR) effect.[8] Among spintronic platforms, magnetic tunnel junctions (MTJs) have emerged as leading candidates for next generation biosensing technologies. Their nanoscale sensitivity to both electronic and magnetic perturbations enable highly precise detection of biomolecular interactions, positioning them as powerful tools for label-free, real-time biomedical diagnostics.

MTJ devices have garnered considerable research interest in recent years due to their potential in spintronic applications. An MTJ typically consists of two ferromagnetic (FM) electrodes separated by a thin non-magnetic insulating or semiconducting (SC) spacer layer, which facilitates quantum mechanical tunneling of spin-polarized electrons.[9,10] The tunneling magnetoresistance (TMR) effect in these structures is strongly dependent on the relative spin alignment of the FM layers parallel (P) or antiparallel (AP) enabling the electrical readout of magnetically encoded information.[11] The TMR ratio is defined as the relative difference in electrical conductance between the P and AP configurations, normalized to the lower conductance state. Remarkably, TMR ratios exceeding 3700% have been experimentally demonstrated in Fe/MgO/Fe and FeCo/MgO/FeCo systems, establishing these junctions as leading candidates for practical device applications.[12–14] Theoretically, TMR ratios can approach infinity when half-metallic ferromagnetic electrodes are employed, due to their complete spin polarization at the Fermi level, making them highly desirable for enhancing device sensitivity.

Heusler alloys, with the general chemical formula X_2YZ, where X and Y are typically transition metals and Z is a main-group element exhibit a wide range of tunable electrical and

---

Microelectronics Lab, James Watt School of Engineering, University of Glasgow, Glasgow, UK

magnetic properties, including half-metallic, semiconducting, and metallic behaviors, depending on their specific composition.[15,16] Among them, cobalt-based full Heusler alloys, such as $Co_2Fe(Si,Al)$, $Co_2(Cr,Fe)Al$, and Co_2MnSi, have attracted significant attention as promising electrode materials due to their high spin polarization and mechanical and thermodynamic stability in spintronic applications.[17] These alloys are often integrated with thin MgO insulating barriers to form MTJs.[18,19] The strong appeal of Co-based full Heusler alloys arises from their high spin polarization and elevated Curie temperatures (Tc), which are essential for maintaining magnetic stability and spin coherence at room temperature.[20] These features make them promising candidates for usage in spintronic devices at room temperature (RT) such as next-generation spintronic biosensors, enabling enhanced sensitivity, reduced signal noise, and cost-effective detection of cancer biomarkers in clinical diagnostics.[21] Recent studies have explored the diagnostic potential of volatile organic compounds (VOCs) as non-invasive biomarkers for cancer detection. Emerging evidence suggests that specific VOC signatures can reliably distinguish breast cancer patients from healthy individuals, reflecting alterations in metabolic pathways associated with tumorigenesis.[22,23] To detect these disease-specific VOCs, a range of sensing technologies has been developed, including electronic noses, gas chromatography mass spectrometry (GC-MS), and nanomaterial-based sensor platforms.[24–26] These approaches have demonstrated improved sensitivity and specificity in identifying VOC profiles associated with cancer, thereby offering promising avenues for early, non-invasive diagnostics. Despite the promise of VOC analysis in cancer diagnostics, significant challenges remain in the standardization of breath sampling protocols and the precise identification of disease-specific VOC biomarkers.[27] In parallel, advancements in spintronic biosensing devices have further enhanced detection capabilities. Conventional single-barrier magnetic tunnel junctions (SB-MTJs), typically fabricated using Fe/MgO/Fe configurations, have demonstrated notable TMR effects and compatibility with established nanofabrication techniques.[28] However, double-barrier magnetic tunnel junctions (DB-MTJs) have recently emerged as promising architectures to surpass the limitations of SB-MTJs. These multilayered structures have shown substantial improvements in TMR performance, with reported increases from 122% to 802% in Fe/MgO/Fe-based systems.[29] The enhancement is primarily attributed to quantum well states and resonant tunneling phenomena that arise within the DB-MTJ structure.[30,31] Furthermore, DB-MTJs exhibit increased sensitivity to interfacial modifications, making them particularly well-suited for biosensing applications where detection of biomolecular interactions at the surface is critical. Notably, the development of iron-free DB-MTJs may also offer additional benefits in biocompatibility and device stability. All these achievements open up avenues for future spintronic device developments, including prospective applications in biosensors.[32]

We explore in this article the possibility of DB-MTJs featuring transition metal dichalcogenides (TMDCs) like MoS_2, and $MoTe_2$ as composite tunnel barriers coupled with Co_2MnSi Heusler alloy electrodes for biosensing applications of high sensitivity. By applying density functional theory (DFT) and nonequilibrium Green's function (NEGF) formalisms, we compute important properties like TMR ratios, transmission spectra, density of states (DOS), and bandgaps for Co_2MnSi–MgO–$MoTe_2$–MgO–Co_2MnSi devices. The obtained TMR ratios is as large as 1226%. These TMR values coupled with the electronically tunable features of TMDCs make DB-MTJs a promising device to identify cancer biomarkers and VOCs in different forms of cancer. The iron-free nature helps to increase longevity through reduced degradation compared to classical Fe-based MTJs, and the increased sensitivity to interfacial variations allows for label-free, non-invasive sensing. The research opens ways to create sophisticated biosensors for the diagnosis of cancer at earlier stages, a versatile, high-performance tool to enhance healthcare and environmental monitoring.

Principle of spintronics devices

TMR is a quantum mechanical phenomenon fundamental to the operation of MTJs, wherein spin-polarized electrons tunnel through an ultrathin insulating barrier, resulting in a resistance that strongly depends on the relative orientation of the FM layers.[11] A typical MTJ comprises two FM electrodes such as Co_2MnSi separated by a nanometer scale insulating barrier,

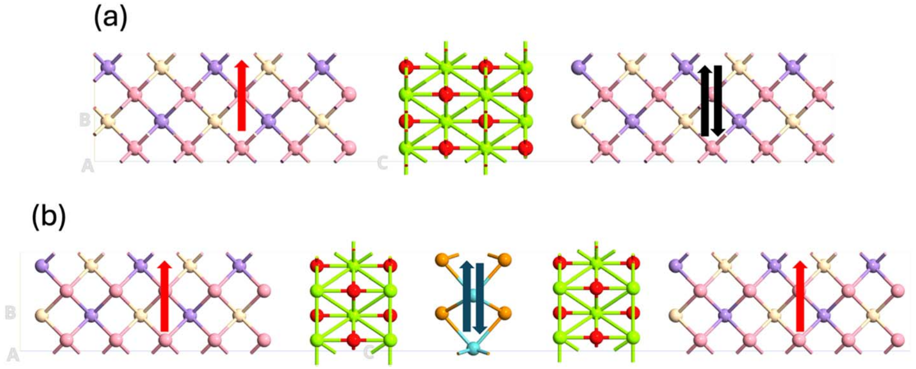

Fig. 1 The structure of magnetization P and AP configuration in MTJ: (a) SB-MTJ and (b) DB-MTJ.

commonly magnesium oxide (MgO), as illustrated in Fig. 1(a). When the magnetizations of the FM layers are aligned in a P configuration, electrons with matching spin orientations tunnel more efficiently, yielding a low-resistance state (R_P). Conversely, in the AP configuration, spin mismatch between the layers significantly reduces tunneling probability, resulting in a high-resistance state (R_{AP}). The schematic arrows in Fig. 1 represent the magnetization directions of the FM layers. In SB-MTJs (Fig. 1(a)), the AP configuration is typically realized by reversing the magnetization of the right FM electrode. In contrast, DB-MTJs (Fig. 1(b)) achieve the AP state by altering the magnetization of the central FM region, thereby enabling more complex spin transport mechanisms.[29] The TMR effect is governed by the spin-filtering mechanism, wherein the conductance of the junction is determined by the spin-dependent density of states (DOS) at the Fermi level of the two FM electrodes. Specifically, the tunneling probability is higher when the spin polarization of both electrodes aligns favorably, enhancing conductance in the P configuration. In contrast, the AP alignment leads to a mismatch in spin states, thereby suppressing electron tunneling. The TMR ratio quantifies the relative change in resistance between the AP and P magnetic configurations and is expressed as:

$$\mathrm{TMR} = \frac{\Delta R}{R_{AP}} = \frac{R_{AP} - R_P}{R_{AP}} \times 100\% \tag{1}$$

Here, R_P and R_{AP} denote the resistance values in the parallel and antiparallel configurations of the MTJ, respectively. Using the Landauer–Büttiker formalism, the zero-bias conductance is given by

$$G = \frac{2e^2}{h} T(E_f)$$

where $T(E_f)$ is the spin-dependent transmission coefficient at the Fermi energy. As $R = 1/G$, we have $R \propto 1/T(E_f)$. Thus, R_P and R_{AP} are computed from the reciprocal of the transmission coefficients at E_f for the respective magnetic configurations.

DB-MTJs offer an advanced architecture to enhance the TMR effect compared to single-barrier MTJs (SB-MTJs). Schematic representations of SB-MTJ and DB-MTJ structures are shown in Fig. 2(a and b) respectively. In the DB-MTJ configuration, two insulating barriers are separated by an intermediate ferromagnetic layer, which may be composed of either the same or different material as the outer ferromagnetic leads. In SB-MTJs, the P and AP magnetic configurations are established by maintaining the magnetization of the left electrode while reversing the magnetization of the right electrode. In contrast, for DB-MTJs, the P and AP states are realized by fixing the magnetization directions of the two outer electrodes and inverting the magnetization of the central ferromagnetic layer. As a result, in the AP configuration of a DB-MTJ, electrons experience spin misalignment at two interfaces during transport, whereas in the P configuration, the spin alignment is preserved throughout the structure. The transmission probability, which quantifies the likelihood of an electron tunneling from the left to the right electrode, is typically higher in the P configuration than in the AP configuration. This leads to a higher TMR ratio in DB-MTJs compared to SB-MTJs. The tunneling process in DB-MTJs is effectively composed of two sequential and independent tunneling events through each barrier. This mechanism is often referred to as sequential independent tunneling, and it significantly enhances the spin-filtering effect, contributing to the superior TMR performance of DB-MTJs.[29]

Simulation methodology

This research discusses the simulation of DB-MTJs as sensitive spintronic for biosensing devices. The mechanism of the sensor relies on the increased TMR effect in DB-MTJs due to optimized material stacks including iron-free ferromagnetic electrodes and 2D-material-based barriers. A larger TMR ratio predicts increased sensitivity of the device toward small electronic or

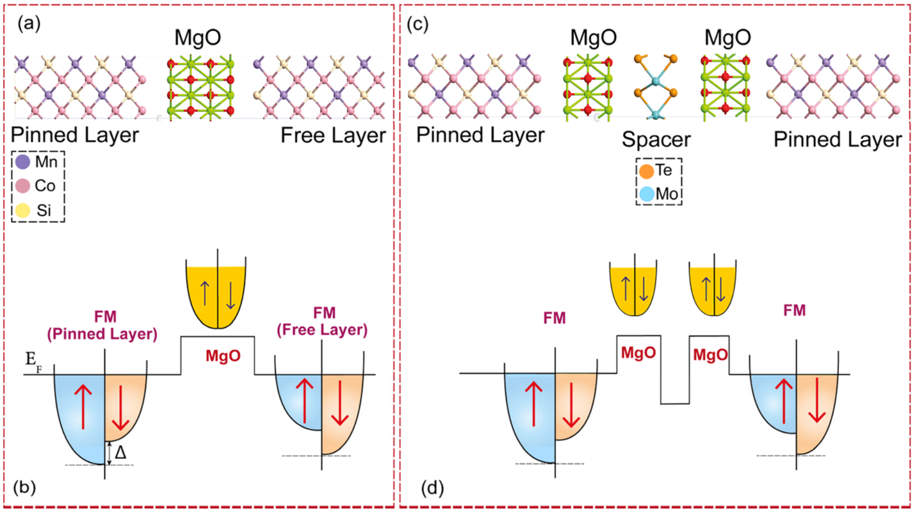

Fig. 2 Schematic of (a and b) single-barrier and (c and d) double-barrier magnetic tunnel junctions (MTJs) with corresponding spin-dependent energy band diagrams.

magnetic perturbations at the junction boundary and therefore makes the structures ideal for biosensing applications.

The suggested DB-MTJ has a symmetric layered configuration, FM/barrier/spacer/barrier/FM (Fig. 1(b)). Wherein the FM electrodes consist of iron-free Heusler alloys (Co_2MnSi), and the MgO as a tunnel barriers comprise insulators merged with semiconducting 2D materials MoS_2, or $MoTe_2$. These DB-MTJ devices in biosensing applications can be coupled with a microfluidic system for the delivery of the analyte toward the sensor surface. As illustrated in Fig. 3, biomarkers binding events linked with specific ligands or antibodies cause local variations in the potential, orientation of dipoles, or the magnetic field, resulting in spin-dependent transport variations in the junction, and this may be measured quantitatively through conductance and TMR variations.

All calculations in this work were performed using DFT employing the linear combination of atomic orbitals (LCAO) method as in Quantum ATK software (version 2023.12). The exchange–correlation potentials were calculated through the generalized gradient approximation (GGA) and the Perdew–Burke–Ernzerhof (PBE) functional.[29] Structural relaxation was attained using geometry optimizations utilizing the limited memory Broyden–Fletcher–Goldfarb–Shanno (LBFGS) method, with a force tolerance of 10^{-4} eV Å^{-1} and a stress tolerance of 0.1 GPa. Transport characteristics were computed using a mixture of DFT and the non-equilibrium Green's function (NEGF) approach, according to the Landauer–Büttiker formalism. Consequently, the MTJ structures were thoroughly optimized at the interfaces between the barrier and electrode, achieving a total energy convergence of less than 10^{-5} eV, with the maximum force on each atom remaining below 0.05 eV Å^{-1}. The optimization was conducted *via* the LBFGS optimizer approach and SGGA exchange–correlation. The *k*-point grid was established at 7 × 7 × 100, and a linear combination of atomic orbitals (LCAO) utilizing single zeta polarization was chosen as the basis set (see Fig. S1 for more details). To calculate band structure, we incorporated GGA-PBE and DFT-1/2 method. Here, 140 hartree was adjusted for cut-off energy of the density mesh with the Monkhorst–pack *k*-point of 13 × 13 × 13.

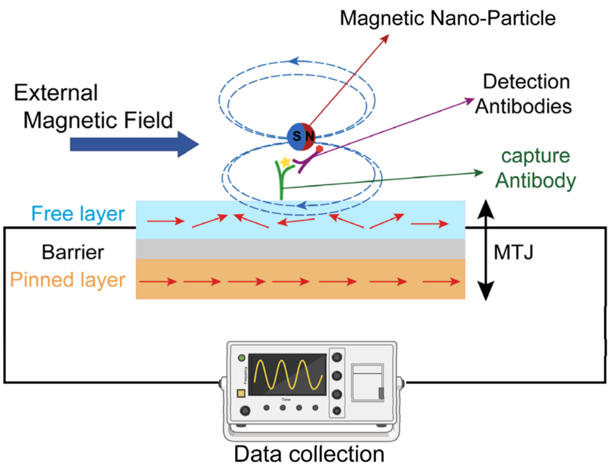

Fig. 3 The mechanism of detection in MTJs devices.

The physical parameters employed for simulations of parallel and anti-parallel configuration simulations are presented in Table 1. The energy convergence criterion for transmission spectrum computations was established at 10^{-5} eV. The obtained transmission spectrum plots are used to calculate the transmission coefficients at the level of the Fermi energy.

Transmission spectra were computed for both parallel and antiparallel magnetic configurations and showed spin polarized transport behaviour and determined the most active tunnelling states. Moreover, the TMR ratio was calculated at the Fermi level. These findings provide the basis for the examination of molecular interaction on the sensor interfaces in modulating spin current transmission.

In addition, DOS and bandgap calculations were also performed for MoS_2, $MoTe_2$, and Co_2MnGe materials. These calculations give insight into the level of spin polarization, the transport channel nature, and the band alignment, which can promote or suppress electron tunnelling. These electronic properties are equally important because they determine how biomarker attachment make changes in dipole orientation, strain, or electrostatic potential, and their effect on the tunnelling probabilities and TMR signal.

This simulation platform develops a firm base for designing and optimizing TMR biosensors through leveraging the increased sensitivity of DB-MTJs toward interface variations. These biosensors will identify biomarkers by quantifiable variations in electronic conductance, spin transport, and pave the way for the development of low-power diagnostic devices for medical and environmental applications.

Results and discussion

TMR ratios and spin-dependent transport

Quantum ATK was employed to calculate the electronic DOS and band structures for all material configurations under both P and AP magnetic alignments. Key transport properties, such as the transmission coefficient, were determined using the non-equilibrium Green's function (NEGF) formalism. Electron tunnelling in these structures is characterized by wave vectors (k_a and k_b) within the scattering matrix framework provided by Quantum ATK, which enables evaluation of electron transmission and reflection probabilities across a range of energy levels.

Specifically, the transmission coefficients at the Fermi level for both P and AP states were extracted from the *k*-resolved

Table 1 Physical parameters utilised for parallel and anti-parallel configurations

Physical parameters	
Broadening temperature	1200 K
Spin	Polarized
Exchange correlation	SGGA (PBE functional)
Density mesh cut-off	140 h
Pseudopotential	SG15
k-Point sampling (*A*, *B*, *C*)	(7, 7, 100)

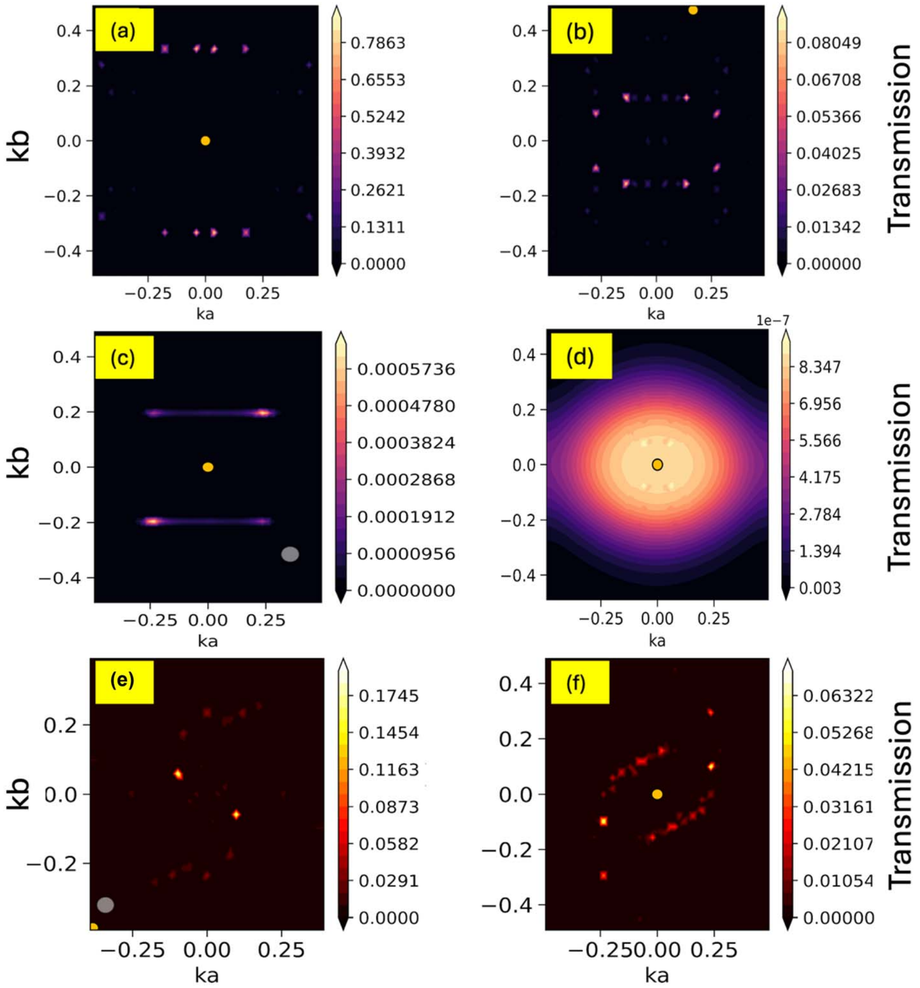

Fig. 4 The *k*-resolved transmission spectrums of $Co_2MnSi-MgO-Co_2MnGe-MgO-Co_2MnSi$ (a) parallel and (b) anti-parallel configuration; $Co_2MnSi-MgO-MoTe_2-MgO-Co_2MnSi$ (c) parallel and (d) anti-parallel configuration, and $Co_2MnSi-MgO-Cu-MgO-Co_2MnSi$ (e) parallel and (f) anti-parallel configurations.

transmission spectra (Fig. 4 and S2) and are summarized in Table 2. Notably, spin-dependent scattering at the interfaces between the FM layers and the insulating barriers significantly influences the tunnelling behaviour. These interfacial effects modulate the spin-polarized transmission pathways, resulting in distinct differences in electron transmission between P and AP configurations, which in turn underlie the observed variations in TMR performance.

The calculated transmission values derived using eqn (2) are consistently higher for the P configurations compared to the AP ones, which aligns with the expected lower electrical resistance in the P alignment due to more efficient spin-aligned electron tunneling.

$$T = \sum_{k} \int_{E_{\min}}^{E_{\max}} T(E,k)\mathrm{d}E \tag{2}$$

where, T denotes transmission coefficients, and $E_{\max}$ and $E_{\min}$ represent the maximum and minimum energies.

Furthermore, Fig. 5 illustrates the electron transmission spectra at the Fermi level for $Co_2MnSi-MgO-Co_2MnGe-MgO-Co_2MnSi$ and $Co_2MnSi-MgO-MoTe_2-MgO-Co_2MnSi$ DB-MTJ structures under total, P, and AP magnetic configurations. The transmission profiles clearly indicate that the P configuration exhibits significantly higher electron transmission, particularly at the Fermi level compared to the AP configuration in both structures. These findings are consistent with the expected spin-dependent tunneling behavior, where the alignment of spin-polarized states in the P configuration facilitates more efficient electron transport. Quantitative values of electron transmission at the Fermi level for each configuration are summarized in Table 2.

The TMR values were calculated using the transmission coefficients obtained for both P and AP magnetic configurations *via* QuantumATK simulations. Eqn (1) was employed to determine the TMR ratio based on these spin-dependent transmission values. The resulting TMR ratios for the DB-MTJs investigated in this study are presented in Table 3. Notably, the $Co_2MnSi-MgO-MoTe_2-MgO-Co_2MnSi$ structure exhibited the highest TMR ratio of 1226.20%, significantly surpassing that of $Co_2MnSi-MgO-MoS_2-MgO-Co_2MnSi$ (TMR = 22%), and

Table 2 Transmission coefficients calculated at a Fermi energy level for parallel and anti-parallel configuration in all MTJs

	Parallel configuration			Anti-parallel configuration		
Device	Spin-up	Spin-down	Total	Spin-up	Spin-down	Total
Co_2MnSi–MgO–Co_2MnGe–MgO–Co_2MnSi	3.72×10^{-5}	1.49×10^{-20}	3.72×10^{-5}	4.85×10^{-6}	1.49×10^{-20}	4.86×10^{-6}
Co_2MnSi–MgO–MoS_2–MgO–Co_2MnSi	6.28×10^{-6}	1.49×10^{-18}	9.57×10^{-8}	9.52×10^{-8}	1.42×10^{-20}	9.52×10^{-8}
Co_2MnSi–MgO–$MoTe_2$–MgO–Co_2MnSi	4.06×10^{-6}	2.79×10^{-9}	4.062×10^{-6}	7.31×10^{-7}	1.63×10^{-18}	3.06×10^{-7}
Co_2MnSi–MgO–Cu–MgO–Co_2MnSi	7.12×10^{-6}	6.75×10^{-13}	7.12×10^{-6}	3.78×10^{-6}	2.12×10^{-18}	3.78×10^{-6}

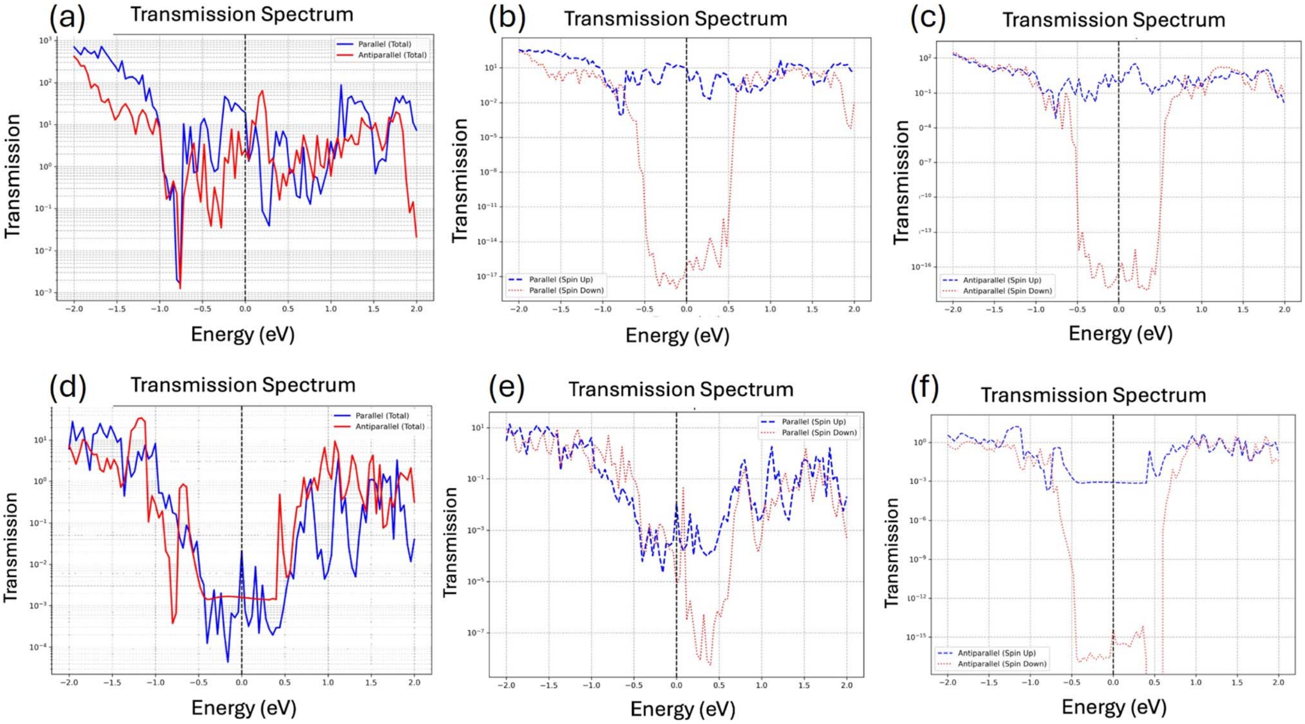

Fig. 5 Transmission spectra of the Co_2MnSi–MgO–Co_2MnGe–MgO–Co_2MnSi at the Fermi level for spin-up and down electrons in total (a), parallel (b) and anti-parallel (c) configurations; Co_2MnSi–MgO–$MoTe_2$–MgO–Co_2MnSi at the Fermi level for spin-up and down electrons in total (d), parallel (e) and anti-parallel (f) configurations.

Co_2MnSi–MgO–Co_2MnGe–MgO–Co_2MnSi (TMR = 667.43%). Additionally, as shown in Fig. 5, the transmission probability at the Fermi level in the P configuration exhibits a substantial increase, reaching 4.06×10^{-6} for spin-up electrons, in contrast to the AP configuration, which yields a significantly lower value of 7.31×10^{-7}. This pronounced difference aligns with the high TMR ratio obtained in this study, further confirming the enhanced spin-polarized transport efficiency in the P state. These findings highlight the critical influence of the spacer material on the spin-dependent transport properties and overall device performance. The substantial variation in resistance between magnetic configurations, as captured by the TMR ratio, serves as a key metric for evaluating and comparing the efficiency of different DB-MTJ architectures (see Fig. S3 for more details of script calculates the TMR).

The integration of $MoTe_2$ as a two-dimensional spacer material within the double tunnel barrier structure (MgO–$MoTe_2$–MgO) appears to enhance spin-dependent tunneling, attributed to its optimal bandgap (~1.1 eV) and intrinsic spin-filtering capabilities, as previously demonstrated for other transition metal dichalcogenides (TMDCs).[33] In comparison, the Co_2MnSi–MgO–Cu–MgO–Co_2MnSi structure yielded a lower TMR ratio of 412%, reinforcing the superior performance of TMDC-based barriers in achieving high TMR values. Notably, a record TMR ratio of 4220.59% was reported by Sinha *et al.* for a Fe–MgO–$MoTe_2$–MgO–Fe-based DB-MTJ, underscoring the beneficial role of $MoTe_2$ in enhancing spin transport due to its

Table 3 TMR ratios of the DB-MTJs

Materials	TMR%
Co_2MnSi–MgO–Co_2MnGe–MgO–Co_2MnSi	667.43
Co_2MnSi–MgO–MoS_2–MgO–Co_2MnSi	22
Co_2MnSi–MgO–$MoTe_2$–MgO–Co_2MnSi	1226.20
Co_2MnSi–MgO–Cu–MgO–Co_2MnSi	421

wide bandgap.[33] However, the use of iron-free Co_2MnSi electrodes in the present study offers distinct advantages, including mitigation of oxidation-related degradation commonly associated with Fe-based systems, thereby improving the long-term stability and reliability of MTJ devices for biosensing applications.

This trend is consistent with the findings reported by Zheng *et al.*, in which Fe/MgO/Fe DB-MTJs exhibited a comparable disparity in electron transmission between the P and AP states, resulting in a TMR ratio of 802%.[29] The enhanced transmission observed in the P configuration can be attributed to the sequential independent tunneling mechanism across the two insulating barriers, which reinforces spin filtering and significantly amplifies the spin-dependent transport characteristics. This mechanism underscores the superiority of DB-MTJs over conventional single-barrier MTJs in achieving higher TMR values and improved sensitivity for spintronic applications. The comparison in TMR ratio of the suggested material structures and reference structures are shown in Table 4.

Density of states and bandgap analysis

Fig. 6 presents the calculated density of states (DOS) and electronic band structures. Analysis of the DOS and band structures reveals that the regions below and above the bandgap are primarily governed by chalcogen p orbitals and transition metal d orbitals, particularly within the valence band. The transition metal d orbitals are the dominant contributors to the bands flanking the bandgap. Due to the d-orbital character of the electronic states near the band edges, the bands in the vicinity of the bandgap appear relatively flat, indicating low dispersion and localized states.

Strong hybridization is observed between the d states of the transition metals and the *s* states of the chalcogen atoms below the Fermi energy level in all structures. Furthermore, when comparing Mo-based chalcogenides from sulfur (S) to tellurium (Te) (Fig. 6(a and b)), a reduction in the bandgap is noted. This trend is attributed to the increasing atomic radii and decreasing electronegativity from S to Te. The electronic states near the Fermi level are primarily derived from Mo d orbitals, and as the ligand field strength of the chalcogen increases (moving from Te to S), broader d-bands are formed, leading to an increased bandgap.

The electrical structure significantly influences the magnetic characteristics of crystalline materials. Consequently, we determined the electronic band structure of the stable phase of the Heusler compound Co_2MnGe utilising polarised spin computations inside the GGA-PBE (Table S1) and DFT-1/2 method. Fig. 6(c) displays the computed dispersion curves along the high symmetry directions of the first Brillouin zone. This figure illustrates that the majority-spin band exhibits overlapping valence and conduction bands, resulting in metallic behaviour, whereas the minority-spin band demonstrates semiconductor characteristics, with the valence band maximum and conduction band minimum located at the Γ and X points, respectively.[35] Fig. 6(d) presents the calculated electronic band structure and calculated DOS for the structure of MgO. The Fermi level located in a broad bandgap, with significant any electronic states immediately near the Fermi energy was observed. This confirms the highly insulating nature of MgO, consistent with its experimentally known bandgap energy of about 6.7 eV. The DOS plot (Fig. 6(d)) illustrates that the occupied states (valence band) and unoccupied states (conduction band) possess a large bandgap, with negligible hybridization close to the Fermi level. The valence band is constituted mainly of oxygen 2p orbitals, whereas the conduction band comprises mainly magnesium 3s orbitals. This bandgap results (Table 5) in the large dielectric breakdown strength and stability of MgO and makes it a favorable material for application as an insulating barrier in MTJs. On the other hand, the Heusler alloy spacer, Co_2MnGe (Fig. 6(c)) is a ferromagnet exhibiting a spin-down bandgap of around ~0 eV.[18] This characteristic guarantees substantial spin polarisation, enhancing the favourable TMR ratio of 667%. The findings underscore the pivotal influence of the spacer material's bandgap on tunnelling efficiency and TMR, with reduced bandgaps often promoting elevated TMR ratios in DB-MTJ systems. Moreover, TMR is not controlled by the barrier bandgap itself, yet greatly tuned by interfacial resonance states, *e.g.*, in (111)-oriented Co/MgO/Co junctions, high TMR ratios are induced by the resonance enhancement of tunneling through one spin channel by interfacial antibonding states which are created close to the Fermi level.[36]

Implications for biosensing applications

The DB-MTJs constructed in this work, notably the Co_2MnSi–MgO–$MoTe_2$–MgO–Co_2MnSi structure with a TMR ratio of 1226%, hold great potential for biosensing to detect early cancer and environmental monitoring. The better performance of the structure based on $MoTe_2$ points to the effectiveness of TMDC-based barriers in facilitating spin-dependent tunneling, which

Table 4 Comparison study of TMR ratio

Structure (this work)	Reference structure	TMR (%)	Ref.
Co_2MnSi–MgO–$MoTe_2$–MgO–Co_2MnSi (TMR% = 1226.20)	Fe–MgO–$MoTe_2$–MgO–Fe	4220.59	33
	Fe–MgO–$MoSe_2$–MgO–CoFeB	2000	33
	CoFe–MgO–MoS_2–MgO–CoFe	1300	33
Co_2MnSi–MgO–Cu–MgO–Co_2MnSi (TMR% = 421)	—	—	—
Co_2MnSi–MgO–Co_2MnGe–MgO–Co_2MnSi (TMR% = 667.43)	Co_2TiGe/MgO/Co_2TiGe	645	34
	Co_2FeAl–2L–MgO–Co_2FeAl	373.27	19
	Co_2TiSi/MgO/Co_2TiSi	1894	34

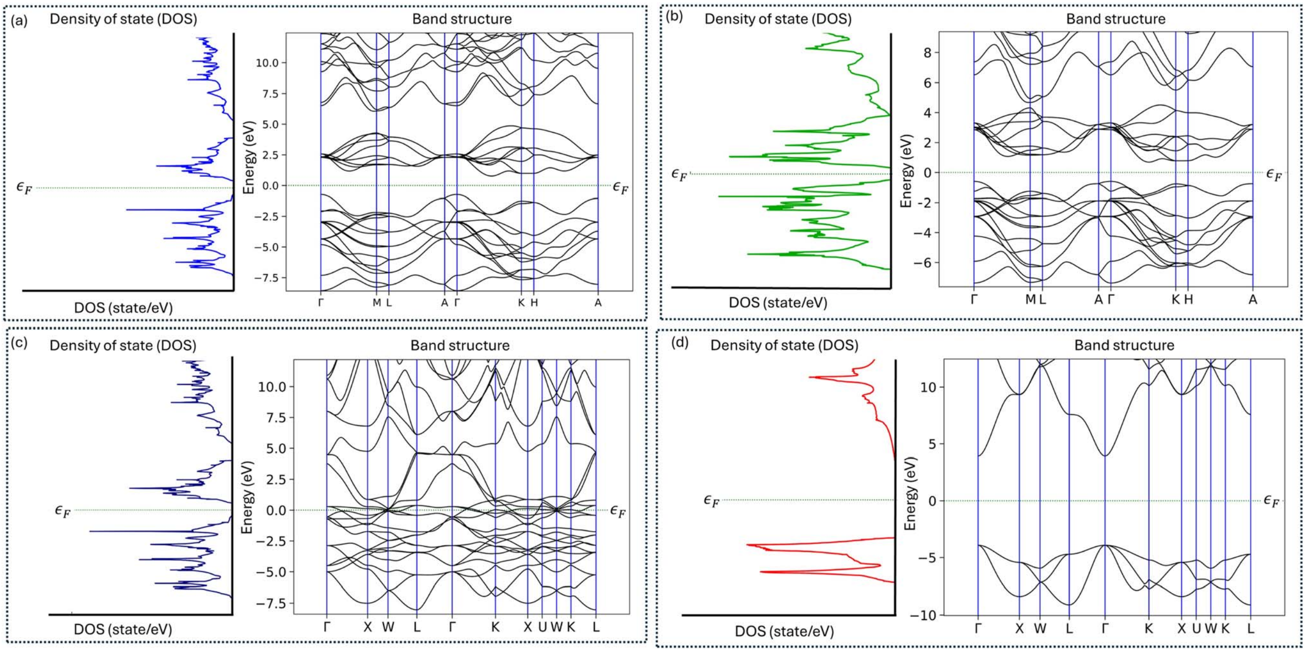

Fig. 6 DOS and Band Structure of MoS_2 (a), $MoTe_2$ (b), Co_2MnGe (c), and MgO (d).

Table 5 Bandgap of spacer materials

Structure	Energy bandgap
MoS_2	1.78 eV
$MoTe_2$	1.11 eV
MgO	6.7 eV
Co_2MnGe	~0 eV

stems from the 1.11 eV bandgap of $MoTe_2$ and the high spin polarization of Co_2MnSi. This sensitivity enables the identification of minor variations in the electronic or magnetic surroundings near the surface caused by the adsorption of cancer biomarkers. The iron-free Co_2MnSi electrodes increase the real-world applicability of all these structures through extended stability and noise reduction, overcoming one of the major limitations of MTJs based on Fe, which suffer from degradation in humid biological solutions. This stability is especially beneficial in clinical applications, where the devices need to function stably even in the presence of biological solutions, and in environmental sensors subject to fluctuating atmospheric conditions, with stable performance over time.

Conclusion

This work illustrates the versatility of double-barrier magnetic tunnel junctions (DB-MTJs) employing transition metal dichalcogenides (TMDCs) as composite tunnel barriers, in conjunction with iron-free electrodes of Co_2MnSi, for potential biosensing application. A TMR ratio of 1226% was obtained for the Co_2MnSi–MgO–$MoTe_2$–MgO–Co_2MnSi structure through the DFT and NEGF simulation, better than other structures of Co_2MnSi–MgO–Cu–MgO–Co_2MnSi (TMR = 412%), Co_2MnSi–MgO–Co_2MnGe–MgO–Co_2MnSi (TMR = 667%), and Co_2MnSi–MgO–MoS_2–MgO–Co_2MnSi (TMR = 22%). The enhanced performance of the $MoTe_2$ structure indicates the efficiency of TMDC-based barriers to boost spin-dependent tunneling owing to the low bandgap of $MoTe_2$ (1.11 eV) and the high spin polarization of the Co_2MnSi electrode. The mechanisms of the observed TMR trends are explained through transmission spectra, and the role of the electronic properties of the spacer material in enabling efficient tunneling has been evidenced through bandgap calculations. The 1226% TMR value is competitive compared to the values from the literature. Compared with previously proposed Heusler-based single-barrier MTJs, the large TMR ratio and interface sensitivity to modifications in the structure of the Co_2MnSi–MgO–$MoTe_2$–MgO–Co_2MnSi make it a potential label-free, non-invasive biosensor to detect cancer biomarkers. Having iron-free electrode material Co_2MnSi ensures device stability and less noise during the measurement, overcoming issues related to iron-based systems and ensuring better stability for biomedical and environmental sensors.

Conflicts of interest

There are no conflicts to declare.

Data availability

No external datasets or code repositories were used or generated during this study.

Supplementary information: simulation parameters and output data. See DOI: **https://doi.org/10.1039/d5ra04973c**.

Acknowledgements

This work was supported by the European Union's Horizon Europe research and innovation programme under the Marie Skłodowska-Curie Doctoral Networks (MSCA-DN) project CanDoIt, grant agreement no. 101120186.

References

1 H. Sung, *et al.*, Global cancer statistics 2020: GLOBOCAN estimates of incidence and mortality worldwide for 36 cancers in 185 countries, *Ca-Cancer J. Clin.*, 2021, **71**(3), 209–249.

2 Y. Wu, *et al.*, Magnetically-driven dual-channel fluorescent biosensor with aptamer logic gates for multiplexed exosomal protein profiling and breast cancer subtyping, *Chem. Eng. J.*, 2025, 164324.

3 Z. Sun, *et al.*, Ratiometric fluorescent biosensor based on self-assembled fluorescent gold nanoparticles and duplex-specific nuclease-assisted signal amplification for sensitive detection of exosomal miRNA, *Bioconjugate Chem.*, 2022, **33**(9), 1698–1706.

4 V. Sanko and F. Kuralay, Label-free electrochemical biosensor platforms for cancer diagnosis: Recent achievements and challenges, *Biosensors*, 2023, **13**(3), 333.

5 L. Syedmoradi, M. L. Norton and K. Omidfar, Point-of-care cancer diagnostic devices: From academic research to clinical translation, *Talanta*, 2021, **225**, 122002.

6 A. Barhoum, Z. Altintas, K. S. Devi and R. J. Forster, Electrochemiluminescence biosensors for detection of cancer biomarkers in biofluids: Principles, opportunities, and challenges, *Nano Today*, 2023, **50**, 101874.

7 Y. Wang, *et al.*, Engineering nanozyme immunomodulator with magnetic targeting effect for cascade-enzyodynamic and ultrasound-reinforced metallo-immunotherapy in prostate carcinoma, *Nat. Commun.*, 2025, **16**(1), 1876.

8 C. Dey, P. Yari and K. Wu, Recent advances in magnetoresistance biosensors: A short review, *Nano Futures*, 2023, **7**(1), 012002.

9 J. Bhattacharya, A. Rawat, R. Pati, A. Chakrabarti and R. Pandey, Spin dependent tunneling and strain sensitivity in a Co 2 MnSb/HfIrSb magnetic tunneling junction: a first-principles study, *Phys. Chem. Chem. Phys.*, 2024, **26**(40), 26064–26075.

10 Z. Cui, *et al.*, Giant tunneling magnetoresistance in two-dimensional magnetic tunnel junctions based on double transition metal MXene ScCr 2 C 2 F 2, *Nanoscale Adv.*, 2022, **4**(23), 5144–5153.

11 V. Nabaei, R. Chandrawati and H. Heidari, Magnetic biosensors: Modelling and simulation, *Biosens. Bioelectron.*, 2018, **103**, 69–86.

12 D. Waldron, V. Timoshevskii, Y. Hu, K. Xia and H. Guo, First principles modeling of tunnel magnetoresistance of Fe/MgO/Fe trilayers, *Phys. Rev. Lett.*, 2006, **97**(22), 226802.

13 S.-Z. Wang and K. Xia, Electric and thermal spin torque across disordered FeCo/MgO/FeCo magnetic tunnel junctions, *Phys. Rev. B*, 2016, **93**(18), 184414.

14 Y. Guo, *et al.*, High thermal stability of perpendicular magnetic anisotropy in the MgO/CoFeB/W thin films, *Appl. Surf. Sci.*, 2021, **568**, 150857.

15 K. Fomina, V. Marchenkov, E. Shreder and H. W. Weber, Electrical and optical properties of X 2 YZ (X = Co, Fe; Y = Cr, Mn, Ti; Z = Ga, Al, Si) Heusler alloys, *Solid State Phenom.*, 2011, **168**, 545–548.

16 Y. Yan, J. Yang, J. Li, Y. Wang and W. Ren, High thermoelectric properties in full-Heusler X2YZ alloys (X = Ca, Sr, and Ba; Y = Au and Hg; Z = Sn, Pb, As, Sb, and Bi), *J. Phys. D: Appl. Phys.*, 2019, **52**(49), 495303.

17 S. Mouchou, Y. Toual, A. Azouaoui, K. Bouslykhane, N. Benzakour and A. Hourmatallah, The effect of temperature on electronic, elastic and thermodynamic properties of Co2MnX (X = Si and Ge), *Phys. B*, 2023, **655**, 414751.

18 T. Aull, E. Şaşıoğlu, N. Hinsche and I. Mertig, Ab initio study of magnetic tunnel junctions based on half-metallic and spin-gapless semiconducting heusler compounds: Reconfigurable diode and inverse tunnel-magnetoresistance effect, *Phys. Rev. Appl.*, 2022, **18**(3), 034024.

19 T. C. Rachakonda, S. P. A. Akhtar and A. Islam, High tunneling magneto-resistance ratio in Co2FeAl Heusler alloy and WSe2 2D material tunnel barrier-based magnetic tunnel junctions, *J. Magn. Magn. Mater.*, 2024, **606**, 172365.

20 Y. Zhao, X. Li, Q. Wu, Y. Feng and B. Wu, Exploring stable half-metallicity and magnetism of Cr-based double half-Heusler alloys and its high magnetoresistance ratio in magnetic tunnel junction, *Mater. Sci. Semicond. Process.*, 2024, **178**, 108415.

21 S. Mostufa, *et al.*, Giant magnetoresistance based biosensors for cancer screening and detection, *ACS Appl. Bio Mater.*, 2023, **6**(10), 4042–4059.

22 D. Speiser, A. Schneider, O. Staeck, C. Freitag, M. Lanowska and M. Mangler, Volatile organic compounds (VOCs) in exhaled breath of patients with breast cancer in a clinical setting, *Ginekol. Pol.*, 2012, **83**(10), 730–736.

23 I. Oakley-Girvan and S. W. Davis, Breath based volatile organic compounds in the detection of breast, lung, and colorectal cancers: a systematic review, *Cancer Biomarkers*, 2018, **21**(1), 29–39.

24 N. Queralto, A. N. Berliner, B. Goldsmith, R. Martino, P. Rhodes and S. H. Lim, Detecting cancer by breath volatile organic compound analysis: a review of array-based sensors, *J. Breath Res.*, 2014, **8**(2), 027112.

25 N. Shehada, G. Bronstrup, K. Funka, S. Christiansen, M. Leja and H. Haick, Ultrasensitive silicon nanowire for real-world gas sensing: noninvasive diagnosis of cancer from breath volatolome, *Nano Lett.*, 2015, **15**(2), 1288–1295.

26 N. Kahn, O. Lavie, M. Paz, Y. Segev and H. Haick, Dynamic nanoparticle-based flexible sensors: diagnosis of ovarian carcinoma from exhaled breath, *Nano Lett.*, 2015, **15**(10), 7023–7028.

27 M. Leemans, P. Bauër, V. Cuzuel, E. Audureau and I. Fromantin, Volatile organic compounds analysis as a potential novel screening tool for breast cancer:

a systematic review, *Biomarker Insights*, 2022, **17**, 11772719221100709.

28 T. Scheike, Z. Wen, H. Sukegawa and S. Mitani, 631% room temperature tunnel magnetoresistance with large oscillation effect in CoFe/MgO/CoFe (001) junctions, *Appl. Phys. Lett.*, 2023, **122**(11), 112404.

29 X. Zheng, S. Yang, Z. Zheng, C.-S. Liu, W. Wang and L. Zhang, Double-barrier magnetic tunnel junctions with enhanced tunnel magnetoresistance, *Appl. Phys. Lett.*, 2024, **125**(22), 223503.

30 Y. Wang, J. Zhang, X.-G. Zhang, H.-P. Cheng and X. Han, First-principles study of Fe/MgO based magnetic tunnel junctions with Mg interlayers, *Phys. Rev. B: Condens. Matter Mater. Phys.*, 2010, **82**(5), 054405.

31 B. Tao, *et al.*, Coherent resonant tunneling through double metallic quantum well states, *Nano Lett.*, 2019, **19**(5), 3019–3026.

32 M. J. Molaei, M. Younas and M. Rezakazemi, A comprehensive review on recent advances in two-dimensional (2D) hexagonal boron nitride, *ACS Appl. Electron. Mater.*, 2021, **3**(12), 5165–5187.

33 R. Sinha and J. Kaur, Enhanced Transport Parameters of Transition Metal Dichalcogenide-Based Double-Barrier Magnetic Tunnel Junction, *J. Electron. Mater.*, 2024, **53**(9), 5505–5518.

34 M. Saleem, *et al.*, Density functional study of electrode material for magnetic tunnel junction designed using Co2TiZ (Z= Ge, Si) heusler alloys, *J. Phys. Chem. Solids*, 2024, **187**, 111868.

35 R. Amraoui, *et al.*, First-principles computational study on structural, elastic, magnetic, electronic, and thermoelectric properties of Co2MnGe: a potential Heusler ternary compound, *Eur. Phys. J. B*, 2022, **95**(12), 198.

36 K. Masuda, H. Itoh and Y. Miura, Interface-driven giant tunnel magnetoresistance in (111)-oriented junctions, *Phys. Rev. B*, 2020, **101**(14), 144404, DOI: **10.1103/PhysRevB.101.144404**.